Investigation of thickness-dependent stress in PbTiO3 thin films

Ausrine Bartasyte, Odette Chaix-Pluchery, Jens Kreisel, Carmen Jiménez, François Weiss, Adulfas Abrutis, Z. Saltyte, Michel Boudard

Investigation of thickness-dependent stress in $PbTiO_3$ thin films

A. Bartasyte [a], O. Chaix-Pluchery, J. Kreisel, C. Jimenez and F. Weiss

Laboratoire des Matériaux et du Génie Physique, CNRS-INP Grenoble, Minatec Bâtiment INPG, parvis Louis Néel, BP 257, 38016 Grenoble Cedex 1, France

A. Abrutis and Z. Saltyte

Dept. of General and Inorganic Chemistry, Vilnius University, Naugarduko 24, LT-03225 Vilnius, Lithuania

M. Boudard

Laboratoire de Science et Ingénierie des Matériaux et Procédés, CNRS-INP Grenoble-UJF, 1130 Rue de la Piscine, BP75, 38402 St. Martin d'Hères Cedex, France

Abstract

X-ray diffraction (XRD) and Raman spectroscopy were used to investigate stress dependence on thickness in $PbTiO_3$ (PTO) films grown by pulsed liquid injection Metalorganic Chemical Vapor Deposition on a $LaAlO_3$ (001) substrate (LAO). Films on sapphire substrate (R-plane) were used as polycrystalline film reference. Epitaxial PTO films with a dominant *c*-domain structure are grown on LAO substrate whereas the films on sapphire are polycrystalline. A detailed investigation of the PTO/LAO film microstructure by XRD gives evidence of PTO twinning. Both techniques reveal that PTO films are under tensile in-plane stresses. The study of the film thickness dependence of microstrains, grain size, volume fraction of *a*-domains as well as surface morphology of PTO/LAO films indicates that these parameters are clearly correlated. A change in the relaxation mechanism between 65 and 125 nm of film thickness has been evidenced. A *c* parameter gradient occurs throughout the film depth; it originates in stress relaxation due to a thickness increase. Raman spectra of PTO films allowed in-plane residual stress values to be estimated from the Raman shifts and are in good agreement with

[a] also at Vilnius University, Dept. of General and Inorganic Chemistry, Naugarduko 24, LT-03225 Vilnius, Lithuania (Corresponding author: Ausrine.Bartasyte@gmail.com).

those determined by XRD. Both techniques also indicate that thinner films are more stressed and residual stresses are partially relaxed with increasing thickness. Moreover, *a*-domains are more stressed than *c*-domains. The two components of the large $A_1(2TO)$ and $A_1(3TO)$ Raman modes have been associated with *a*- and *c*-domains and their intensity ratio clearly correlated with the volume fraction of *a*-domains.

I. Introduction

Thin films of $PbTiO_3$ (PTO) and other related ferroelectric materials offer key advantages for a variety of applications in non-volatile ferroelectric random access memories, microelectronics, and sensors technologies[1]. The physical properties of ferroelectric thin layers are substantially different from those of bulk ferroelectrics, due to substrate – film interactions, grain size effects, defects.[2,3] Film stresses can significantly change mechanical, optical and electrical properties, domain structure formation, and the nature of phase transition in ferroelectric films,[4,5] which in turn has a potential influence on the reliability of devices. Therefore, the investigation of residual stress helps in predicting physical properties for ferroelectric film – based devices. Optical fluorescence,[6] X-ray diffraction (XRD),[7] wafer curvature measurements,[8] cantilever beam deflection,[9] laser reflectance,[10] and Raman spectroscopy[11-17] have been used for stress analysis in ferroelectric materials. Among them, XRD and Raman spectroscopy are most popular, as they are powerful tools for the non-destructive investigation of structure. Raman spectroscopy is complementary to XRD methods as it is a local probe and sensitive to even subtle changes of symmetry. Moreover, Raman modes are strongly influenced by mechanical deformation of the sample such as hydrostatic pressure or stress.[18-21]

Films are submitted to substantial stresses during growth and subsequent cooling process from deposition temperature to room temperature (RT). At the growth temperature, stresses are mainly misfit stresses (also called epitaxial stresses) which result from lattice mismatch between the film and substrate. Intrinsic stresses related to the growth technique are negligible in Metalorganic Chemical Vapor Deposition (MOCVD). During the cooling process, additional stresses may develop in the film, either due to thermal stress arising from different film and substrate thermal expansion coefficients or to stress related to the structural phase transition. Stresses in $PbTiO_3$ thin films are mainly relaxed by dislocations and by twins forming at and below the cubic to tetragonal phase transition. The distribution and volume fraction of twins depend on the substrate nature and film thickness[22] and on the cooling rate from the deposition temperature.[23]

Even though epitaxial films often have physical properties superior to those of polycrystalline films (i.e. in terms of polarization), only a few papers on stress evaluation by Raman spectroscopy are known in such films;[15,16] most reports concern stress evaluation in polycrystalline films on sapphire or Si substrates.[11-14] Different theoretical studies analyse the stress state[24] and the possible mechanisms for stress relaxation[23] in epitaxial PTO thin films.

Here we report a systematic study of stress and domain structure evolution as a function of film thickness for PTO films by using XRD, Raman spectroscopy and atomic force microscopy (AFM).

II. Experimental details

A. Film deposition

Film depositions were carried out in a vertical hot wall pulsed injection MOCVD reactor described elsewhere.[25-27] The injector injects microdroplets (a few microliters) of an organic solution containing a dissolved mixture of metalorganic precursors. After flash evaporation of the microdroplets, the resulting vapour mixture is transported by an Ar + O_2 gas flow towards the heated substrate. The injector consists of a computer-driven high-speed precision electromagnetic valve operating under a repetitive pulsing regime. The deposition conditions were optimized (see Table 1) in order to obtain a pure and high quality PTO perovskite phase on two different single crystalline substrates: $LaAlO_3$ (LAO) with the surface cut parallel to a (00l) plane (indices refer to the pseudocubic setting, a=3.791 Å)[28] and sapphire with the surface cut parallel to a rhombohedral *R*-plane (a=3.5 Å)[29]. Corresponding misfit strains between tetragonal PTO and LAO (SAPH) substrate at RT are -2.8% (-11.4 %) and -9.6 % (-18.7 %) with the PTO *a*-axis a_t and *c*-axis c_t, respectively (bulk PTO lattice parameters: a_t =3.899 Å and c_t =4.153 Å)[30]. Such considerations using PTO bulk parameters suggest that PTO films are under compressive in-plane stress for both Al_2O_3 and LAO substrates.

Standard film characterisation by scanning electron microscopy (SEM) and XRD shows a high quality single phase film. More details concerning the deposition technique and standard sample characterisation can be found in Ref. 31.

Films of different thickness were deposited on LAO at 650°C and then slowly cooled at a rate of 2 °/min; the thicknesses correspond roughly to 30, 65, 125, 250 and 460 nm as measured from film cross-sectional micrographs obtained by SEM. Naturally cooled (10-20 °/min) PTO films deposited on LAO and SAPH, 250 nm of thickness, were also analysed.

B. Film analysis

The surface morphology of the different films was examined by AFM using a Digital Instruments Multimode Scanning Probe Microscope, in the tapping mode. The film texture and microstructure were studied by XRD in Schulz and Bragg-Brentano geometries using a SIEMENS D5000 4-circle diffractometer with monochromatic CuK_α radiation (λ = 0.15418

nm). An analysis of the microstructure of epitaxial films was carried out through standard ω-, χ- and ϕ-scans and pole figures. The proportion of *c*- and *a*-domains was quantified as the percentage of *a*-domains (*A*, %) in the films and was calculated by peak integration of the (102) reflection in ϕ-scans corresponding to the different domains:

$$A = \frac{2(I(102)_{\chi=58} + I(102)_{\chi=62})}{2(I(102)_{\chi=58} + I(102)_{\chi=62}) + I(102)_{\chi=27}} \quad (1)$$

where $I(102)$ is the peak area in ϕ-scans measured at different χ angles, corresponding to *a*-axis and *c*-axis oriented crystallites (i.e. *a*- and *c*-domains). Lorentz-polarization and absorption corrections were not applied.

Raman spectra were collected using a Jobin Yvon/Horiba LabRam spectrometer equipped with a liquid nitrogen cooled charge coupled device detector. Experiments were conducted in the micro-Raman mode at RT in a backscattering geometry. The 514.5 nm line of an Ar^+ ion laser was focused to a spot size smaller than 1 μm. Spectra from different experiments are calibrated using Si spectra at RT.

III. Results

A. X-ray diffraction

Typical θ/2θ XRD patterns of PTO films deposited on LAO (PTO/LAO) and SAPH substrate (PTO/SAPH) are shown in Fig. 1a and Fig. 1b, respectively. The XRD pattern of the 250 nm thick PTO/LAO film is characteristic of the PTO tetragonal structure with a high degree of preferred orientation consisting only of intense (00*l*) and very weak (*h*00) reflections (Fig.1 a). This indicates a dominant *c*-domain structure containing a small fraction of *a*-domains. PTO/SAPH films are polycrystalline with a slightly (101) preferred orientation (Fig. 1b).

The full width at half maximum (FWHM) value of the rocking curve (ω-scan) measured on the (001) PTO/LAO reflection varies between 0.3° and 1.0° in the 30 - 460 nm range of film thickness as shown in Table 2. As expected, the 00*l* texture is more pronounced in thinner films. The ϕ-scans performed from the (102) reflection of *a*- and *c*-domains and of the substrate confirm a cube on cube epitaxial growth of PTO/LAO. Taking into account the influence of twinning and instrumental resolution (0.1° in ω-scan, 0.5° in ϕ-scan) on FWHM values given in Table 2, the PTO/LAO films can be considered as rather well-oriented films.

An investigation of the PTO/LAO film microstructure gives evidence of twinning through peak splitting in (102) pole figures: therefore, the *c*-axis (*a*-axis) of the tetragonal unit cell in *c*-domains (*a*-domains) is tilted by a small angle from the film-substrate plane. More details about texture and domain structure are given in Ref. 31. An evaluation of the volume fraction of twinned *a*-domains according to Eq. (1) is given in Table 2 and Fig. 2 for PTO/LAO films of different thickness.

Fig. 3 shows the evolution of the (002) reflection line as a function of film thickness. The analysis of the line profile indicates an important line broadening in all films and an increase of the corresponding d_{002} values due to an increase with thickness of the *c*-parameter in *c*-domains determined from the five (00*l*) reflections (Table 2). The lowest *c* value is observed for the thinnest film and gradually increases with increasing film thickness without reaching the bulk *c* value (Fig. 3). Compressive stress in the [00*l*] direction, dominant in the substrate/*c*-domains interface region, could explain such a difference with bulk values. However, thin films are usually considered as subjected to biaxial stresses in the film plane whereas the normal direction is stress-free. Therefore, the *c* parameter decrease in *c*-domains should rather arise from biaxial tensile stress in the film plane although a compressive stress is expected from lattice mismatch.

In the case of the tetragonal *c*-axis oriented thin film on cubic substrate, the film is under biaxial stress σ_b in the basal *xy* plane and z direction is stress free. Therefore, the principal stress components are equal $\sigma_{xx}=\sigma_{yy}=\sigma_b$ and there are no shear stress/strain components. For symmetry reasons, the basal strain is also biaxial $\varepsilon_{xx}=\varepsilon_{yy}=\varepsilon_b$. Considering the tensor relationship between stresses and strains expressed with Hooke's law, the mechanical equilibrium relation is obtained:

$$\begin{pmatrix} \sigma_b \\ \sigma_b \\ 0 \end{pmatrix} = \begin{pmatrix} C_{11} & C_{12} & C_{13} \\ C_{12} & C_{11} & C_{13} \\ C_{13} & C_{13} & C_{33} \end{pmatrix} \begin{pmatrix} \varepsilon_b \\ \varepsilon_b \\ \varepsilon_{zz} \end{pmatrix} \quad (2)$$

where C_{ij} are the terms of the elastic stiffness matrix. Then, the biaxial stress σ_b can be expressed as a function of the strain in the z direction (ε_{zz}) from Eq. (2) as:

$$\sigma_b = \left(-\frac{(C_{11}+C_{12})C_{33}}{2C_{13}} + C_{13} \right) \varepsilon_{zz} \quad (3)$$

the strain ε_{zz} being calculated from the film and bulk PTO *c* lattice parameters.

The residual stress values in PTO/LAO films estimated from Eq. (3) (C_{11}=237 GPa, C_{33}=60 GPa, C_{12}=90 GPa and C_{13}=70 GPa)[32] are given in Table 3. The positive stress values

σ_b suggest that the films are under tensile stress in the film plane although a compressive stress is expected from lattice mismatch. Residual stress gradually relaxes from 1 to 0.4 GPa with increasing film thickness from 30 to 460 nm.

Reflection profiles of the 250 and 460 nm films present a marked asymmetry on the low *d* side which we attribute to a *c* parameter gradient throughout the film depth. The *c* values, smaller near the substrate–film interface than at the free surface of the film, are directly related to a stress gradient throughout the film depth due to relaxation. As a consequence, all films are expected to present a similar *c* parameter at a given distance from the film substrate. A detailed analysis of lattice parameters in all films is in progress and results will be reported in a forthcoming paper.

A line broadening may originate in strain and size effects. For instance, the FWHM observed for the 125 nm film is almost three times larger than the instrumental resolution (0.17 ˚2θ evaluated from the substrate line profile). The individual contributions from strain and size to the (00*l*) reflection line broadening were estimated using both the Williamson-Hall analysis (WH)[33] and the Halder-Wagner approximation (HW).[34] The deconvolution of the instrumental contribution and profile fitting using a pseudo-Voigt function approximation were carried out using the program *WinplotR*.[35] Calculations were performed using the five (00*l*) reflections and results are given in Fig. 4. Both methods give the same tendency: the average grain size increases with film thickness, and is close to the thickness value in thinner film (Fig. 4a). Values obtained by the WH analysis are in the 20-135 nm range against 18-75 nm when using the HW approximation. Microstrains first decrease with film thickness reaching a minimum value (0.8 % in WH and 1.8 % in HW analysis) between a thickness of 65 and 125 nm and then increase again (up to 1.4 % in WH and 2.9 % in HW analysis) (Fig. 4b). The same evolution of microstrains was reported by de Keijser *et al* in PTO/$SrTiO_3$ films.[36] Microstrain values are estimated as rather high values and comparable to reported ones[36]. Both analyses converge and give evidence that the line broadening is mainly due to strain effect but grain size effect cannot be neglected especially in thinner films.

B. Film morphology

The surface morphology of PTO/SAPH and PTO/LAO films was observed by AFM. As shown in Fig.5 and Fig. 6, a different morphology is observed depending on the cooling rate of the films. The films obtained after natural cooling process (10-20 °/min) have a very smooth surface and present a tweed pattern morphology characteristic of a twinning relaxation mechanism with perpendicular lines of *a*-domains and larger rectangular zones of

c-domains (Fig. 5a). A slow cooling rate initiates dislocations, reducing the formation of twinned *a*-domains. For example, in the 250 nm PTO/LAO film, the fraction of *a*-crystallites decreases from 29 % to 14.5 % when the cooling rate is reduced to 2 °/min. Then, stress relaxation in slowly cooled films takes place through the formation of more dislocations. The surface morphology of such films consists mainly of spherical grains (250 and 460 nm in Fig. 6). This morphology is typical of films deposited by MOCVD which grow by an island growth mechanism with high growth rates. Such a morphology was also observed for polycrystalline PTO films on SAPH as shown in Fig. 5b.

The evolution of film surface morphology of slowly cooled PTO/LAO layers as a function of film thickness is given in Fig. 6. The film surface is progressively affected by twinning up to 125 nm of thickness. A further increase in the film thickness results in a surface composed of spherical grains.

C. Raman spectroscopy

1. Effect of polarization and scattering geometry

Polarized Raman spectra given in Figs. 7a and 7b confirm that PTO/LAO and PTO/SAPH films consist of a well crystallized single PTO tetragonal phase. The spectra were recorded on the film surface, i.e. the direction of the incident and scattered laser beam is normal to the substrate plane. As expected from the C_{4v} point group selection rules,[37] only *E(TO)* modes are observed in the PTO/LAO spectrum recorded in crossed polarization configuration (VH) (Fig. 7a). The spectrum measured in parallel polarization configuration (VV) contains a mixture of $A_1(TO)$, $A_1(LO)$, *E(TO)* and *E(LO)* modes instead of the only allowed $A_1(TO)$ modes; this is related to the existence of domains leading to laser depolarization. Considering the thin film orientation and Raman selection rules, it follows that *E(TO)* and $A_1(TO)$ modes, respectively observed in VH and VV configurations, come from *a*-domains.

In the case of PTO/SAPH, A_1 and E modes are observed whatever the polarization configuration but the A_1 and *E(LO)* intensities decrease in VH geometry in comparison with VV configuration and they do not completely disappear (Fig. 7b). This indicates that films on SAPH are rather polycrystalline with only a minor preferred orientation.

A second scattering geometry with the incident and scattered laser beams parallel to the substrate plane was used ("cross section spectra" in the following): the spectra recorded in this geometry in VH (VV) configuration consist also of *E(TO)* ($A_1(TO)$) modes which come from

c- and *a*-domains. Considering that the *c*-domain fraction is at least 80 % whatever the film thickness, we can assume that these modes come mainly from *c*-domains.

2. Effect of thickness

E(TO) modes and residual stress

The measurements of PTO/LAO polarized Raman spectra also permit us to isolate the low-frequency *E(1TO)* soft mode from the very intense LAO A_{1g} soft mode (123 cm^{-1}) which entirely covers it in spectra recorded without polarization selection.

In 250 nm thick PTO/SAPH and PTO/LAO films, the *E(1TO)* soft mode is observed well below that observed in bulk PTO (89.5 cm^{-1}), at roughly 83 cm^{-1} in the case of SAPH substrate and at 87 cm^{-1} in the case of LAO substrate. The fact that all *E(TO)* modes, including the *E(3TO)* hard mode, also shift towards low-wavenumbers in each spectrum (Table 4) suggests that PTO films are under tensile stress whatever the SAPH or LAO substrate, in agreement with XRD results.

As reported in earlier studies,[18] the *E(1TO)* soft mode is pressure sensitive and, as a consequence, it shifts in wavenumber as a function of increasing pressure as follows:

$$\omega[E(TO)] = \omega_0[E(TO)] + (\delta\omega[E(TO)]/\delta P)P \quad (4)$$

where $\omega_0[E(1TO)]$ = 89.5 cm^{-1} is the soft mode wavenumber at zero pressure and room temperature, and $\delta\omega[E(1TO)]/\delta P$ = -5.8 ± 0.2 cm^{-1} GPa^{-1} is the pressure coefficient.[18] Although the biaxial strain of thin films cannot be directly compared with the effect of hydrostatic pressure, the band shift offers an evolution of the residual stress in compressively strained thin films. Let us however parenthesize that Eq. (4) is used in the literature regardless of the stress state (compressive and tensile)[11,12,14,16,38] and this although the pressure coefficient is experimentally known only for compression. As a matter of fact, it is difficult to anticipate the tensile pressure coefficient for an anharmonic soft mode from compression data. Furthermore, the soft mode should shift to lower frequencies by the size effect.[39] As a consequence of this we chose to estimate the stress also from the shift of *E(3TO)* which is a real (harmonic) hard mode in the sense that its pressure coefficient is positive ($\delta\omega[E(3TO)]/\delta P$ = +7.1 ± 1 cm^{-1} GPa^{-1})[18]. We expect that this mode offers a more reliable estimation of the stress. Stress values obtained from the *E(1TO)* soft mode and *E(3TO)* hard mode by using Eq. (4) are given in Table 3. This equation is reasonably usable in the case of PTO/LAO films as reported in Ref. 40.

Corresponding stress values in PTO/SAPH and PTO/LAO calculated from Eq. (4) are closed to 1.1 and 0.4 GPa using *E(1TO)* and to 0.3 and 0.6 GPa using *E(3TO)*, respectively. As exposed above, we believe that the values derived from the *E(3TO)* hard mode are more reliable, and thus the stress values of PTO/SAPH films are rather close to 0.3 GPa. The latter is confirmed by the fact that the measured *c* lattice parameter of films on LAO and SAPH are almost the same (4.119±0.005 Å and 4.114±0.005 Å, respectively). The stress values related to 50-950 nm thick polycrystalline films were reported by different authors to be in the range of 2.6-0.9 GPa.[11,12,14,38,41,42] Dobal *et al.* reported a higher stress value (1.5 GPa) for the 250 nm PTO/SAPH film[14] compared with our measured value (0.3 GPa). The stress was measured as high as 2 GPa in epitaxial 250 nm thick PTO/MgO films.[16] Stress values estimated in our films are rather lower than the literature values but we note that literature studies use only the disputable *E(1TO)* soft mode (which we have also calculated for comparison with the literature values, Table 3). However, let us emphasize again that stresses are not only dependent on the lattice mismatch but are highly sensitive to the deposition method and experimental conditions.

The Raman spectra of 250 nm thick PTO/LAO films recorded for *a*- and *c*-domains using both scattering geometries are given in Fig. 8a. It appears that the deviation from the single crystal wavenumbers of *E(1TO)* as well as that of the other *E(TO)* modes is more important in *a*-domains than in *c*-domains. Fig. 8b and 8c show the evolution of the profile of the *E(1TO)* soft mode measured in both types of domains as a function of PTO/LAO film thickness; the Raman shifts of *E(1TO), E(2TO)* and *E(3TO)* are given in Table 4. The deviation from the bulk values, just as the stress, increases as thickness decreases. Corresponding stress values estimated from Eq. (4) using *E(1TO)* and E*(3TO)*, when possible, are given in Table 3. Indeed, the *E(3TO)* mode is partially masked by the intense A_1*(3TO)* PTO and E_g LAO modes in the thinner films in the case of *a*-domains. In Fig. 9 we compare stress values measured by XRD with values obtained by the hard *E(3TO)*; it can be seen that there is a good agreement between both techniques, which further validates the reliability of the *E(3TO)* mode. Moreover, as mentioned above for a 250 nm thick film, *a*-domains are more stressed than *c*-domains: stress values in *c*-domains estimated from the *E(3TO)* Raman shift are in the range of 0.7-0.5 GPa against 1.2-0.8 GPa in *a*-domains as thickness increases from 125 to 460 nm. Such a difference can be explained by a larger lattice mismatch with the substrate in *a*-domains and by the fact that they form thin sheet zones in a matrix of *c*-domains,[22,43] which in turn generates a supplementary strain at *c*/*a* domain interfaces. Similar results were obtained

by Lee *et al.* in PTO/MgO epitaxial films[16] despite a reverse mismatch between PTO and MgO lattice parameters as compared with those of PTO and LAO.

As observed in Fig. 8c, a second weak component is also observed in *E(1TO)* (shown with an asterisk) as well as in *E(2TO)* in *a*-domains in films thinner than 460 nm. Unlike the main component, it shifts towards higher wavenumbers when the film thickness decreases. Although our Raman study does not allow a clear interpretation of this observation, we suggest that this might be related to stress or optical effects; complementary work is in progress to check this hypothesis.

PTO/LAO depolarized Raman spectra of high-wavenumber modes as a function of film thickness are given in Fig. 10. All modes are systematically shifted towards higher wavenumbers in comparison with those in VH spectra. This shift can be explained by a change in relative intensities between each *E(TO)* mode and its corresponding oblique modes.[44] This high complexity of such depolarized spectra implies that one should record VH spectra in order to obtain well defined *E(TO)* mode profiles. Just as for the B_1+*E* mode, it is pointed at 290.1 cm^{-1} whatever the film thickness (Fig. 10). Note that it is a degenerate silent mode; however, the polarized Raman spectra in Fig. 7a indicate that the *E* mode can be entirely isolated from the B_1 mode in VH geometry, as previously observed by Lee *et al.*[16]

Domains and A_1(TO) modes

The second A_1*(1TO)* soft mode in PTO/LAO has not been accurately observed due to the too close LAO soft mode. A_1*(2TO)* and A_1*(3TO)* modes appear as very large bands split into two components corresponding to *a*- and *c*-domains in VV spectra recorded on film surface, labeled a and c in Fig. 10, whose intensity ratio varies with film thickness. As already mentioned, A_1*(TO)* modes arise from *a*-domains in spectra collected on the film surface and the presence of *c*-domain A_1*(TO)* modes results from depolarization. The separation of modes coming from both *a*- and *c*-domains is not easy, as the *a*-domain fraction is quite small, thus *c*-domain A_1*(TO)* modes may have higher intensity than *a*-domain modes. Nevertheless, A_1*(TO)* modes coming from different domains can be separated because the intensity of A_1*(TO)* modes related to *c*-domains highly increases in spectra recorded on the cross section. Also these modes can be assigned to *a*- and *c*-domains from other observations.

First, *a*-domains are more stressed than *c*-domains which results in lower wavenumbers for a-component. Second, the intensity ratio between a- and c-components is correlated with the volume fraction of *a*-domains as attested in Fig. 10; it follows the same thickness dependence, a- being the more intense component in the 125 nm thick film spectrum (Fig.

10). In a recent study of $Pb(Zr,Ti)O_3$ /MgO epitaxial films,[45] a remarkable correlation is found between the $A_1(1TO)$ mode intensity and the *c*-domains volume fraction, thus providing a simple probe for domain characterization. However, although the $A_1(TO)$ modes come from both *a*- and *c*-domains according to Raman selection rules, the authors in Ref. 45 have not considered the *a*-domain contribution to the $A_1(TO)$ mode intensity.

IV. Discussion and concluding remarks

XRD and Raman spectroscopy were used to investigate the stress dependence on thickness in $PbTiO_3$ films grown by pulsed liquid injection MOCVD on $LaAlO_3$ (001) substrate. Both techniques reveal that the films are under tensile stress in the film plane although a compressive stress is expected from mismatch with the substrate. Residual stress values obtained from the Raman shifts of the $E(3TO)$ hard mode are in good agreement with the values calculated from the *c* parameters measured by XRD in *c*-domains. They are strongly thickness dependent: thinner films are more stressed and residual stresses are partially relaxed with increasing film thickness. However, very thin films are affected by compressive misfit stress unfavouring *a*-domain formation, whereas they are under high tensile residual stress; this results in high microstrains in the film. An increase of thickness up to 125 nm leads the film to be less substrate dependent which allows some tensile stress relaxation by twinning (*a*-domain formation). As a consequence, microstrains decrease and *a*-domain fraction increases modifying the film morphology. A further increase of film thickness up to 460 nm leads to a change in the dominant relaxation mechanism from twinning to dislocation formation; the film surface is then composed of spherical grains and the *a*-domain fraction starts to decrease. The increase of dislocation concentration results in higher disorder and thus, in increasing microstrains. Residual stress values also indicate that *a*-domains are more stressed than *c*-domains.

The origin of the tensile residual stress is not only the mismatch between the film and the substrate. Other possible origins of tensile stress are related to phase transition and to difference in film and substrate thermal expansion coefficients. Thermal stresses are rather small in PTO/LAO films, thus the high residual stress values, especially in thinner films, cannot be explained if the stress related to the phase transition is assumed to be completely relaxed (or to be stress free). To conclude, residual stress measured at RT is the sum of all stresses developed during the complex process of film preparation, and it cannot be associated to only one origin of stress.

Complementary XRD and TEM measurements are in progress. They are essential for a more complete study of lattice parameters, and then of stresses, and `of twinning in PTO films as a function of film thickness.

Acknowledgments: This work has been financially supported by the European network of excellence FAME and EGIDE.

References

[1] J.F. Scott, Ferroelectr. Rev. **1,** 1 (1998).

[2] M. Okuyama and Y. Hamakama, Sens. Mater. **1**, 13 (1988).

[3] J.F. Scott and C.A. Paz de Araujo, Science **246**, 1400 (1989).

[4] S.B. Desu, Phys. Status Solidi A **141**, 119 (1994).

[5] S.S. Sengupta, D. Roberts, J.-F. Li, M.C. Kim, and D.A. Payne, J. Appl. Phys. **78**, 1171 (1995).

[6] Q. Ma and D.R. Clarke, J. Am. Ceram. Soc. **76**, 1433 (1993).

[7] E. Ching-Prado, A. Reynes-Figueroa, R.S. Katiyar, S.B. Majimder, and D.C. Agrawal, J. Appl. Phys. **78**, 1920 (1995).

[8] C.C. Li and S.B. Desu, J. Vac. Sci. Technol. A **14**, 1 (1996).

[9] J.H.L. Voncken, C. Lijzenga, K.P. Kumcer, K. Kiezer, A.J. Burggraaf, and B.C. Benekamp, J. Mater. Sci**. 27**, 472 (1992).

[10] S.S. Sengupta, S.M. Park, D.A. Payne, and L.H. Allen, J. Appl. Phys. **83**, 2291 (1998).

[11] D. Valim, A.G. Sauza Filho, P.T.C. Freire, J. Mendes Filho, C.A. Guavany, R.N. Reispaud, and E.B. Araujo, J. Phys. D: Appl. Phys. **37**, 744 (2004).

[12] D. Fu, T. Ogawa, H. Suzuki, and K. Ishikawa, Appl. Phys. Lett. **77**, 1532 (2000).

[13] A.-D. Li, D. Wu, C.-Z. Ge, P. Lu, W.-H. Ma, M.-S. Zhang. C.-Y. Xu, J. Zuo, and N.-B. Ming, J. Appl. Phys. **85**, 2146 (1999).

[14] P.S. Dobal, S. Bhaskar, S.B. Majamder, and R.S. Katiyar, J. Appl. Phys. **86**, 828 (1999).

[15] L. Sun, Y.F. Chen, L. He, C.-Z. Ge, D.-S. Ding, T. Yu, M.-S. Zhang, and N.B. Ming, Phys. Rev. B **55**, 12218 (1997).

[16] S.-H. Lee, H.M. Jang, S.M. Cho, and G.-C. Yi, Appl. Phys. Lett. **80**, 3165 (2002).

[17] H. Zheng, J. Kreisel, Y.H. Chu, R. Ramesh, and L. Salamanca-Riba, Appl. Phys. Lett. **90**, 113113 (2007).

[18] J.A. Sanjurjo, E. Lopez-Cruz, and G. Burns, Phys. Rev. B **28**, 7260 (1983).

[19] F. Cerdeira, W.B. Holzapfel, and D. Bauerle, Phys. Rev. B **11**, 1188 (1975).

[20] I.A. Kornev, L. Bellaiche, P. Bouvier, P.E. Janolin, B. Dkhil, and J. Kreisel, Phys. Rev. Lett. **95**, 196804 (2005).

[21] I.A. Kornev and L. Bellaiche, Phase Transitions **80**, 385 (2007).

[22] S. Stemmer, S.K. Streiffer, F. Ernst, M. Ruhle, W.-Y. Hsu, and R. Raj, Solid State Ionics **75**, 43 (1995).

[23] J.S. Speck and W. Pompe, J. Appl. Phys. **76**, 466 (1994).

[24] W.K. Choi, S.K. Choi, and H.M. Lee, J. Mater. Res. **14**, 4677 (1999).

[25] J.P. Sénateur, F. Weiss, O. Thomas, R. Madar, and A. Abrutis, Patent FR2707671 (1993), PCT FR94/00858 (1994), US5945162 (1999), Eu EP730671 (1996).

[26] J.P. Sénateur, A. Abrutis, F. Felten, F. Weiss, O. Thomas, and R. Madar, In "Advances in Inorganic Films and Coatings" Ed. P. Vincenzin (Techna srl., Italy, 1995).

[27] J.P. Sénateur, C. Dubourdieu, V. Galindo, F. Weiss, and A. Abrutis, in "Innovative processing of films and nanocrystalline powders" Ed. K.-L. Choy, (Imperial College Press, London, 2002).

[28] S.A. Hayward, F.D. Morrison, S.A.T. Redfern, E.K.H. Salje, J.F. Scott, K.S. Knight, S. Tarantino, A.M. Glazer, V. Shuvaeva, P. Daniel, M. Zhang, and M.A. Carpenter, Phys. Rev. B **72**, 054110 (2005).

[29] T. Huang, W. Parish, N. Masciocchi, and P. Wang, Adv. X-ray Anal. **33**, 295 (1990).

[30] U.S. National Bureau of Standards, Circ. 359, 5, 39 (1955).

[31] A. Bartasyte, A. Abrutis, C. Jimenez, F. Weiss, O. Chaix-Pluchery, and Z. Saltyte, Ferroelectrics **353**, 104 (2007).

[32] A.G. Kalinichev, J.D. Bass, B.N. Sun, and D.A. Payne, J. Mater. Res. **12**, 2623 (1997).

[33] G.K. Williamson and W.H. Hall, Acta Metall. **1**, 22 (1953).

[34] N.C. Halder and C.N.J. Wagner, Acta Crystallogr. **20**, 312 (1966).

[35] T. Roisnel and J. Rodriguez-Carvajal, Mat. Sci. Forum, Proc. 7th Eur. Powder Diffraction Conference (EPDIC 7) (2000) 118, Ed. R. Delhez and E.J. Mittenmeijer.

[36] M. de Keijser, D.M. de Leeuw, P.J. van Veldhoven, A.E.M. De Veirman, D.G. Neerinck, and G.J.M. Dormans, Thin Solid Films **266**, 157 (1995).

[37] M.D. Fontana, H. Idrissi, G.E. Kugel, and Wojcik, J. Phys.:Condens. Matter **3**, 8695 (1991).

[38] T. Ohno, D. Fu, H. Suzuki, H. Migazaki, and K. Ishikawa, J. Eur. Ceram. Soc. **24**, 1669 (2004).

[39] W. Ma, M. Zhang, and Z. Lu, Phys. Status Solidi A **166**, 811 (1998).

[40] A. Bartasyte, O. Chaix-Pluchery, J. Kreisel, J. Santiso, S. Margueron, M. Boudard, C. Jimenez, A. Abrutis, and F. Weiss, IEEE Trans. Ultrason. Ferroelectr. Freq. Control 54, 2623 (2007).

[41] W. Ma, M. Zhang, T. Yu, Y. Chen. and N. Ming, Appl. Phys. A **66**, 345 (1998).

[42] I. Taguchi, A. Pignolet, L. Wang, M. Proctor, F. Levy, and P.E. Schmid, J. Appl. Phys. **73**, 394 (1993).

[43] C.S. Ganpule, V. Nagarajan, B.K. Hill, A.L. Roytbard, E.D. Willians, S.P. Alpay, A. Roelops, R. Waser, and L.M. Eng, J. Appl. Phys. **91**, 1477 (2002).

[44] C.M. Foster, Z. Li, M. Grimsditch, S.-K. Chan, and D.J. Lam, Phys. Rev. B **48**, 10160 (1993)

[45] M. Osada, K. Nishida, S. Wada, and T. Katoda, Appl. Phys. Lett. **87**, 232902 (2005).

Tables

Table 1: General conditions of $PbTiO_3$ deposition by PI-MOCVD

Substrates	$LaAlO_3$ (001); Sapphire (R-plane)
Substrate temperature, °C	650
Evaporation temperature, °C	280
Transport gas	$Ar + O_2$
Total gas flow rate, l/h	60
Oxygen flow rate, l/h	24
Pressure, Torr	10
Precursors	$Pb(thd)_2$; $Ti(thd)_2(O^iPr)_2$[a]
Solvent	toluene
Solution concentration (total), mol/l	0.04
Injection frequency, Hz	2
Growth rate, nm/h	~ 1160
Thickness, nm	30- 460
Cooling rate	2°/min until 400 °C

[a] thd – 2,2,6,6-tetramethyl-3,5-heptanedionate, O^iPr – i-propoxide

Table 2: XRD characterisation of PTO/LAO films of various thicknesses

Film thickness (nm)	460	250	125	65	30
Volume fraction of *a*-domains (%)	4.7	14.5	19.4	9.0	-[a]
FWHM of (001) ω-scan (°)[b]	1.0	0.9	0.8	0.7	0.3
FWHM of (102) ϕ-scan (°)[b]	1.9	2.0	2.2	1.7	1.8
c-lattice parameter (Å) (±0.005 Å) in *c*-domains	4.130	4.119	4.107	4.094	4.093

[a] Undetermined due to very low peak intensities

[b] *c*-domains

Table 3: Residual stress values determined from the *c* lattice parameters in *c*-domains obtained by XRD and from the Raman shift of *E(1TO)* and *E(3TO)* modes in PTO/LAO films of different thicknesses.

Film thickness (nm)		30	65	125	250	460
Residual stress value in *c*-domains (GPa)	XRD	1.02 ± 0.15	1.00 ± 0.14	0.79 ± 0.11	0.58 ± 0.08	0.40 ± 0.06
	E(1TO)	1.10 ± 0.35	0.81 ± 0.17	-	0.43 ± 0.09	0.36 ± 0.04
	E(3TO)	1.30 ± 0.21	0.88 ± 0.14	0.70 ± 0.11	0.59 ± 0.10	0.45 ± 0.07
Residual stress value in *a*-domains (GPa)	*E(1TO)*	1.97 ± 0.34	1.71 ± 0.17	0.64 ±0.09	0.60 ± 0.09	0.53 ± 0.04
	E(3TO)	-	-	1.15 ± 0.16	0.95 ± 0.16	0.76 ± 0.12

Table 4: *E(1TO*), *E(2TO)* and *E(3TO)* phonon wavenumbers in PTO single crystal, 250 nm thick PTO/SAPH and PTO/LAO films of different thicknesses. Both PTO single crystal and PTO/LAO thin films have the same ferroelectric 180º and 90º domain structure. The *a*- and *c*-domain values were obtained from film surface and cross-sectional spectra recorded in VH polarization configuration, respectively.

	Thickness (nm)	ω (*E(1TO)*) (cm^{-1})		ω (*E(2TO)*) (cm^{-1})		ω (*E(3TO)*) (cm^{-1})	
Bulk PTO	-	89.5		219.9		506.2	
PTO/SAPH	250	83.1		207.8		504.3	
		a-domains	*c*-domains	*a*-domains	*c*-domains	*a*-domains	*c*-domains
PTO/LAO	460	86.4	87.4	210.5	214.6	500.8	503.0
PTO/LAO	250	86	87.0	208.8	212.4	499.4	502.0
PTO/LAO	125	85.8	-	206.5	-	498	501.2
PTO/LAO	65	79.6	84.8	204.3	208.6	-	499.9
PTO/LAO	30	78.1	83.1	204.3	204.3	-	496.9

Figure captions

Fig. 1: θ/2θ X-ray diffraction pattern of 250 nm thick (a) PTO/LAO and (b) PTO/SAPH films.

Fig. 2: Film thickness dependence of *a*-domain volume fraction in PTO/LAO films.

Fig. 3: Film thickness evolution of the (002) reflection line in the XRD pattern of PTO/LAO films. The d_{002} value of PTO single crystal is indicated as a dashed line.

Fig. 4: Film thickness evolution of (a) average grain size and (b) microstrains in *c*-domains along the [001] direction as obtained by Williamson–Hall and Halder-Wagner analyses.

Fig. 5: AFM images (2x2 μm^2) of 250 nm thick (a) PTO/LAO and (b) PTO/SAPH films. Cooling rate after deposition was 10-20 ^{o}/min.

Fig. 6: AFM images (1x1 μm^2) of PTO/LAO films of various thicknesses (tilted images are given in the insets for 250 and 460 nm thick films). Average roughness values (Ra) are indicated for each film thickness. Cooling rate after deposition was 2 ^{o}/min.

Fig. 7: Polarized Raman spectra of 250 nm thick (a) PTO/LAO and (b) PTO/SAPH films recorded on film surface in parallel (VV) and crossed (VH) polarization configurations.

Fig. 8: (a) Comparison of Raman spectra measured on film surface (*a*-domains) and on cross section (*c*-domains) in VH polarization configuration. The wavenumbers of *E(1TO)*, *E(2TO)* and *E(3TO)* modes in PTO single crystal are shown as dashed lines. The film thickness evolution of the *E(1TO)* soft mode recorded on cross section and on film surface in VH configuration is given in (b) and (c), respectively.

Fig. 9: Film thickness evolution of the residual stress values in *c*-domains calculated from *c* lattice parameters (XRD) and from Raman shifts of *E(3TO)* Raman mode.

Fig. 10: Film thickness dependence of PTO/LAO depolarized Raman spectra. The evolution of the intensity ratio between a- and c-components of the split $A_1(3TO)$ mode as a function of *a*-domain volume fraction in PTO/LAO is given in the inset.

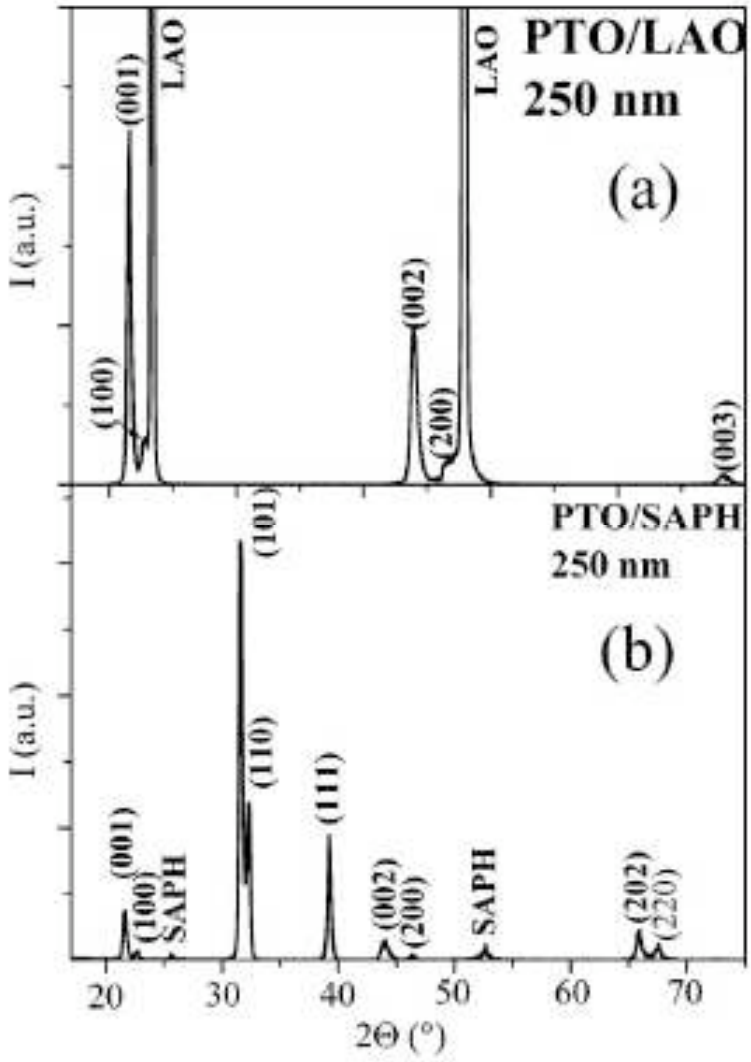
PTO/LAO
250 nm
(a)
I (a.u.)
(001)
LAO
(100)
(002)
(200)
LAO
(003)
PTO/SAPH
250 nm
(b)
I (a.u.)
(101)
(110)
(111)
(001)
(100)
SAPH
(002)
(200)
SAPH
(202)
(220)
20
30
40
50
60
70
2Θ (°)

Fig. 1

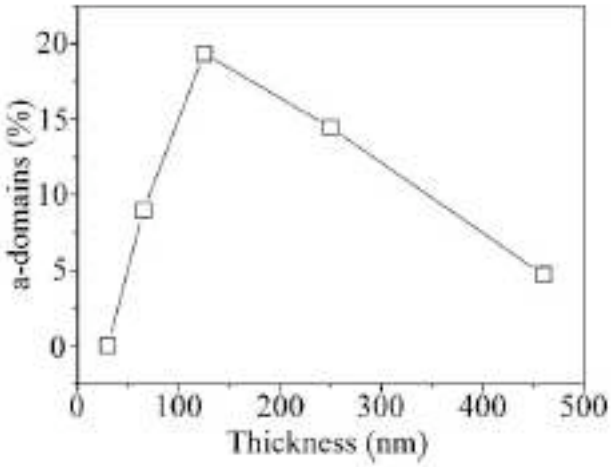

Fig. 2

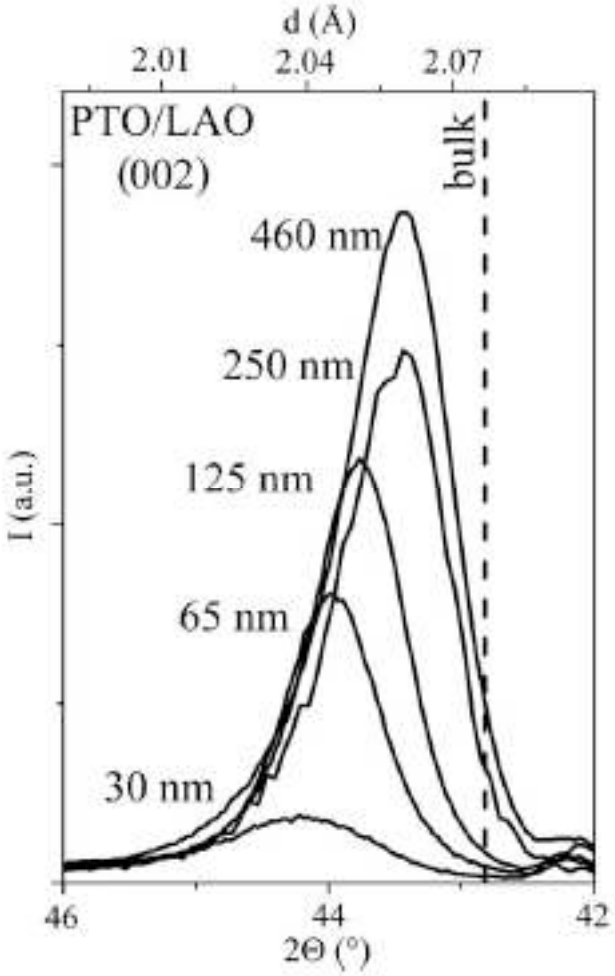
d (Å)
2.01
2.04
2.07
PTO/LAO
(002)
bulk
460 nm
250 nm
125 nm
65 nm
30 nm
I (a.u.)
46
44
42
2Θ (°)

Fig. 3

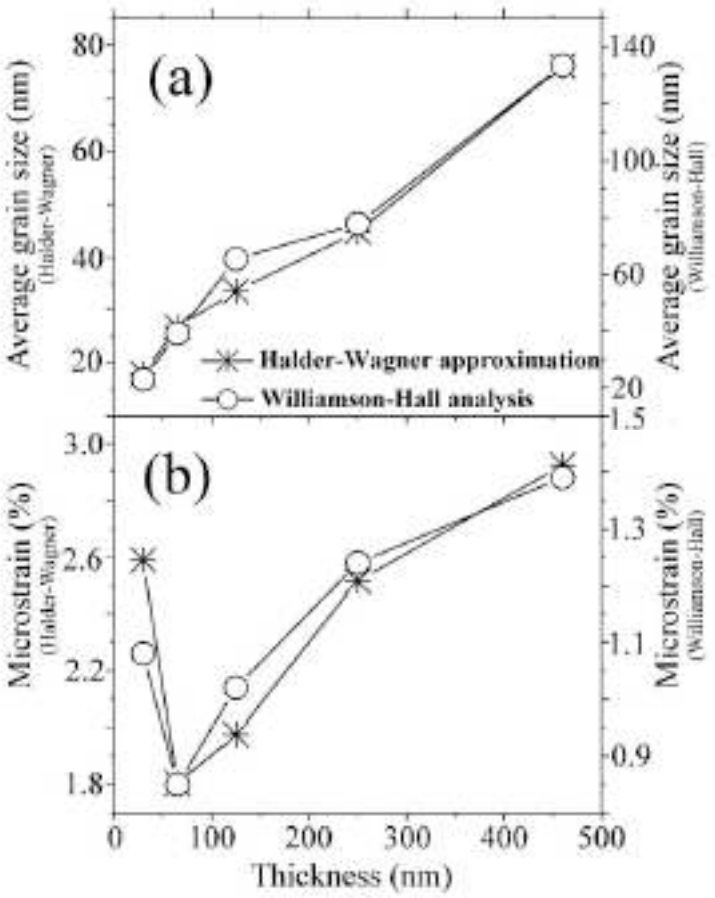
(a)
(b)
Average grain size (nm)
(Halder-Wagner)
Average grain size (nm)
(Williamson-Hall)
Halder-Wagner approximation
Williamson-Hall analysis
Microstrain (%)
(Halder-Wagner)
Microstrain (%)
(Williamson-Hall)
Thickness (nm)
80
60
40
20
140
100
60
20
3.0
2.6
2.2
1.8
1.5
1.3
1.1
0.9
0
100
200
300
400
500

Fig. 4

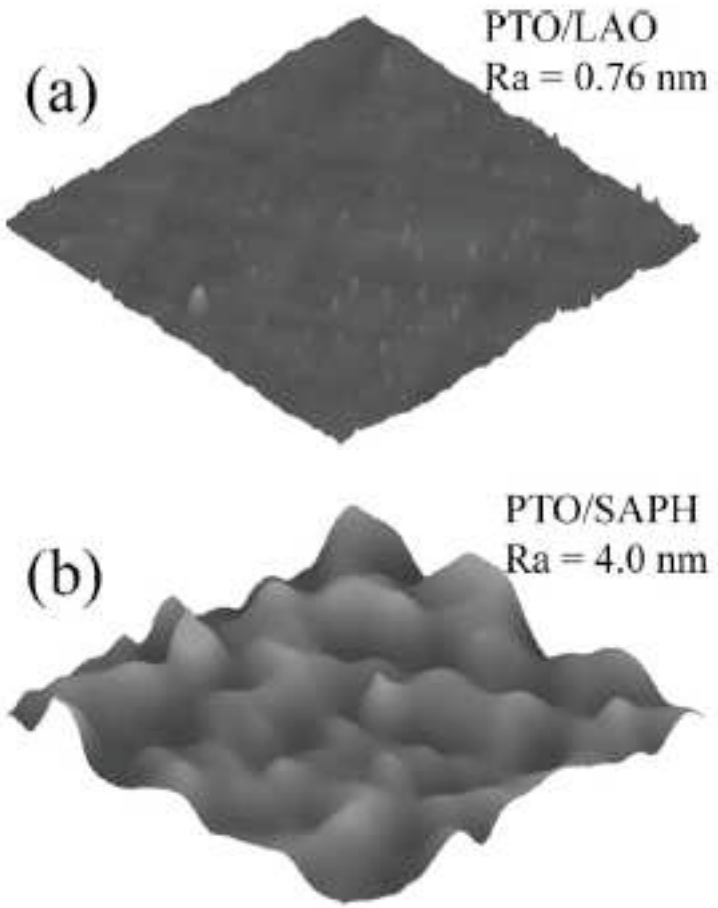

Fig. 5

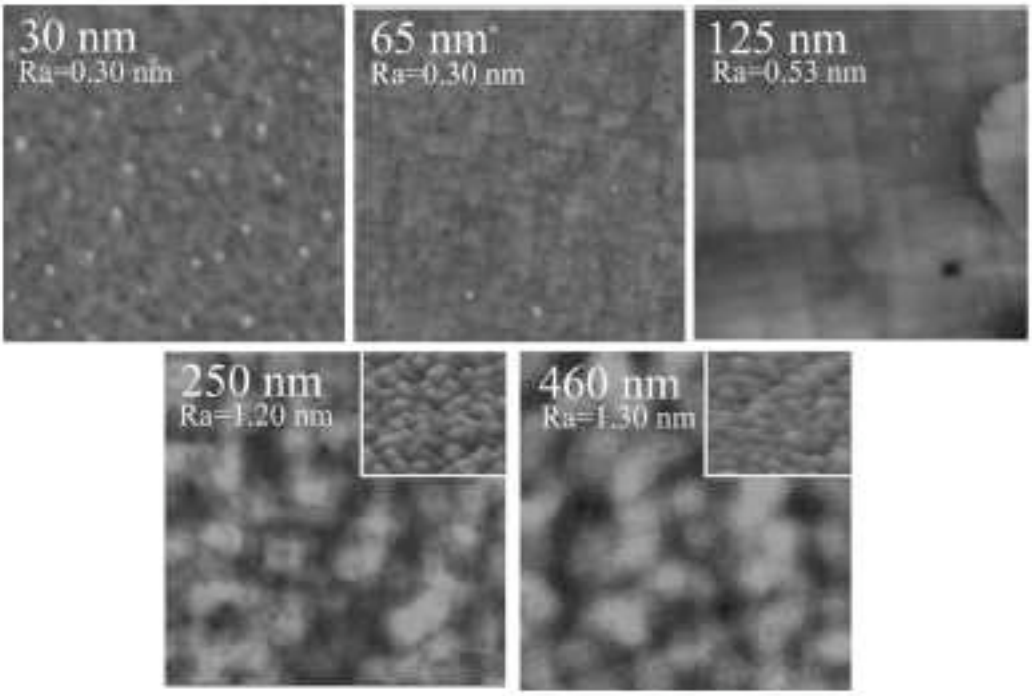
30 nm
Ra=0,30 nm
65 nm
Ra=0,30 nm
125 nm
Ra=0,53 nm
250 nm
Ra=1,20 nm
460 nm
Ra=1,30 nm

Fig. 6

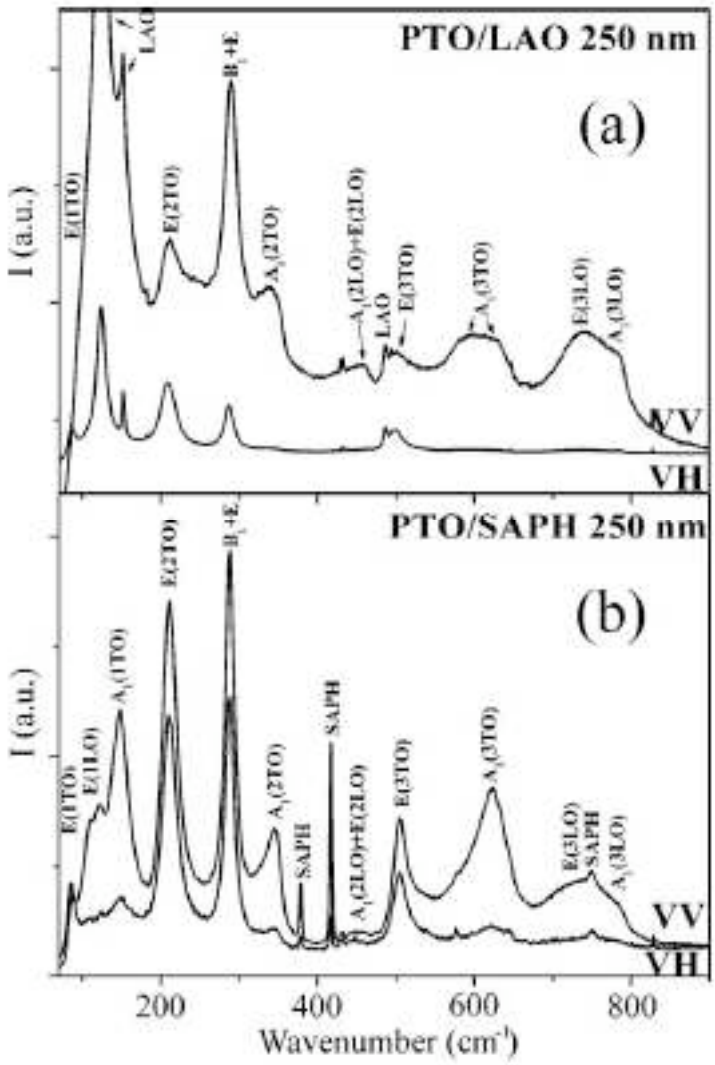
PTO/LAO 250 nm
(a)
I (a.u.)
E(1TO)
LAO
E(2TO)
B1+E
A1(2TO)
A1(2LO)+E(2LO)
LAO
E(3TO)
A1(3TO)
E(3LO)
A1(3LO)
VV
VH
PTO/SAPH 250 nm
(b)
I (a.u.)
E(1TO)
E(1LO)
A1(1TO)
E(2TO)
B1+E
A1(2TO)
SAPH
SAPH
A1(2LO)+E(2LO)
E(3TO)
A1(3TO)
E(3LO)
SAPH
A1(3LO)
VV
VH
200
400
600
800
Wavenumber (cm-1)

Fig. 7

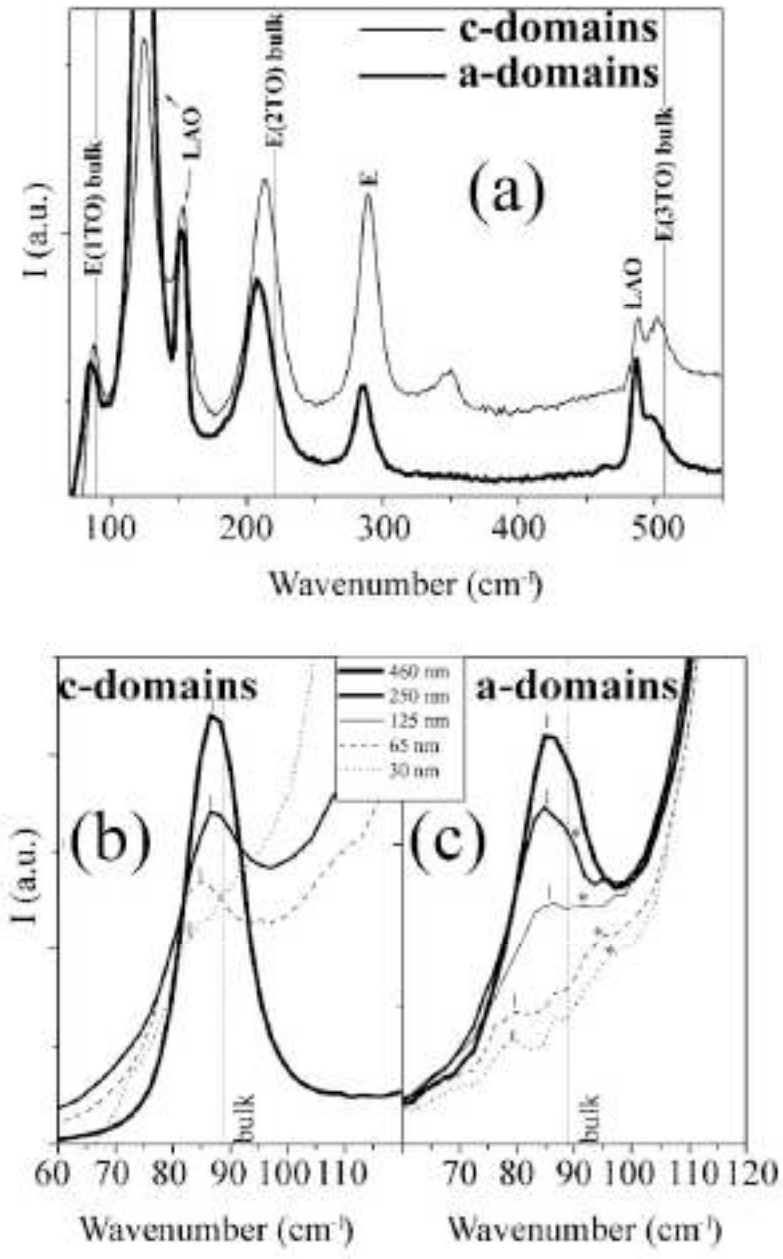
c-domains
a-domains
E(1TO) bulk
LAO
E(2TO) bulk
E
(a)
LAO
E(3TO) bulk
I (a.u.)
100
200
300
400
500
Wavenumber (cm-1)
c-domains
460 nm
250 nm
125 nm
65 nm
30 nm
a-domains
(b)
(c)
I (a.u.)
bulk
bulk
60 70 80 90 100 110
70 80 90 100 110 120
Wavenumber (cm-1)
Wavenumber (cm-1)

Fig. 8

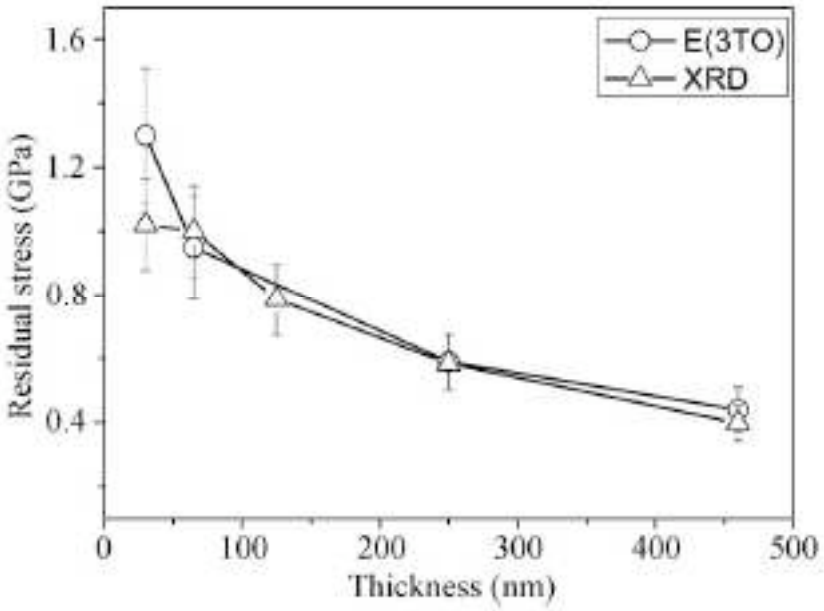
E(3TO)
XRD
Residual stress (GPa)
1.6
1.2
0.8
0.4
0
100
200
300
400
500
Thickness (nm)

Fig. 9

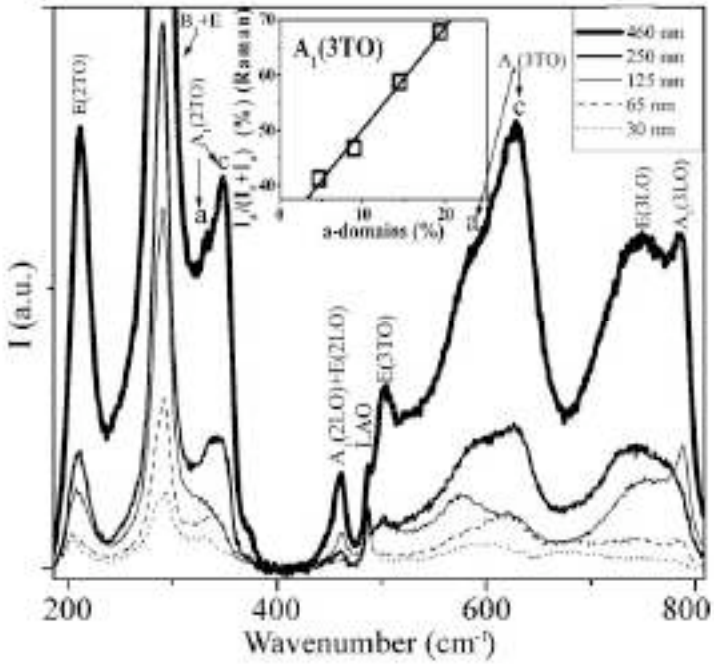
460 nm
250 nm
125 nm
65 nm
30 nm
E(2TO)
B1+E
A1(2TO)
a
c
A1(3TO)
c
E(3LO)
A1(3LO)
A1(2LO)+E(2LO)
LAO
E(3TO)
I (a.u.)
200
400
600
800
Wavenumber (cm-1)
A1(3TO)
a-domains (%)

Fig. 10